Materials Advances

ROYAL SOCIETY OF CHEMISTRY

PAPER

View Article Online
View Journal | View Issue

Cite this: *Mater. Adv.*, 2024, 5, 8490

Rapid microwave synthesis of medium and high entropy oxides for outstanding oxygen evolution reaction performance†

Muhammad Asim,[a] Akbar Hussain,[a] Sadia Kanwal,[a] Awais Ahmad,[b] Yasemin Aykut,[c] Ayşe Bayrakçeken[c] and Naveed Kausar Janjua *[a]

The development of efficient and durable catalysts for the oxygen evolution reaction (OER) is urgent for renewable and sustainable energy storage and conversion. High-entropy oxides (HEOs) have gained significant attention for OER electrocatalysis owing to their multielement synergy and tunable electronic structure. The presence of multiple cations and anions in HEOs' crystal structure leads to a slow diffusion effect, lattice distortion, high configurational entropy, and cocktail effect. The high configurational entropy of HEOs reveals outstanding electrochemical activity due to the large number of active sites compared with their individual counterparts. Herein, a series of equimolar (quaternary, quinary, and senary) and non-equimolar HEOs were fabricated using a rapid microwave irradiation method. The crystal structure, morphology, elemental composition and oxidation states of the HEOs were explored *via* different physical characterizations. The OER activity of the HEOs was investigated through cyclic voltammetry (CV), linear sweep voltammetry (LSV), chronoamperometry, and electrochemical impedance spectroscopy (EIS). All the prepared HEOs demonstrated outstanding OER activity, where the optimum composition exhibited a low overpotential of 350 mV, Tafel slope of 49.4 mV dec^{-1} at 10 mA cm^{-2} and excellent stability for 3600 s. Other electrocatalytic parameters including high diffusion coefficient (D°) (2.2 × 10^{-8} cm^2 s^{-1}), mass transport coefficient (m_T) (2.9 × 10^{-4} cm s^{-1}), heterogeneous rate constant (k°) (5.85 × 10^{-4} cm s^{-1}), high active surface area (A) (0.0116 cm^2), and turnover frequency (TOF) (1.388 s^{-1}) were observed for optimized composition. EIS analysis revealed low solution resistance and charge transfer resistance values. This outstanding performance is attributed to multiple cationic contribution due to the synergistic effect, high durability, improved conductivity, and high entropy stabilization. However, the electrochemical behavior of HEOs depends on each metal ion and its concentration on the catalyst's surface, thus providing new opportunities for tailoring their functional properties by simply changing their elemental composition for different electrochemical applications.

Received 30th June 2024,
Accepted 14th September 2024

DOI: 10.1039/d4ma00667d

rsc.li/materials-advances

1. Introduction

The development of cutting-edge research procedures and the groundwork for materials with unique properties and capabilities are two main approaches for advancement in materials science. A revolutionary approach known as "high entropy" gained significant popularity because it offers a distinct opportunity to discover and tune properties of materials that were previously unattainable, spanning the complete periodic table.[1,2] The process of material design based on the high-entropy concept makes the formation of a single-phase system composed of 5 or more principal elements possible. These materials differ from a doped system where the concentration of the dopant is restricted and destabilization can occur if the concentration surpasses a specific threshold.[3,4] A high-entropy system can be described in two ways: based on its composition and configurational entropy. Based on the composition, high-entropy materials are composed of five or more principal elements with 5–35 wt% contribution. The configurational entropy of these materials is greater than 1.5R (where R is the general gas constant), irrespective of whether these are single phase or multiphase solid solutions. These special compounds are classified into low entropy ($\leq 1R$), medium entropy (1–1.5R)

[a] *Department of Chemistry, Quaid-i-Azam University, Islamabad 45320, Pakistan. E-mail: nkausarjanjua@yahoo.com*
[b] *Department of Chemistry, The University of Lahore, Lahore, Pakistan*
[c] *Faculty of Engineering, Department of Chemical Engineering, Atatürk University, Erzurum 25240, Turkey*

† Electronic supplementary information (ESI) available. See DOI: https://doi.org/10.1039/d4ma00667d

and high entropy ($\geq 1.5R$) materials depending on their configurational entropy.[5]

In 2004, Yeh *et al.*[6] and Cantor *et al.*[7] reported the first high-entropy material composed of five principal metal atoms, known as a high-entropy alloy (HEA). Advance studies on the development of HEAs have revealed that these materials have unique properties compared to conventional alloys because of four core effects, *i.e.*, high configurational entropy, lattice distortion, hysteresis diffusion, and cocktail effect.[1,8] The concept of high entropy is broadened now, and various types of high entropy materials (including high entropy carbides, sulfides, nitrides, silicides, diborides, and oxides) have been reported.[9–14] These HEMs have a wide range of potential applications in electrocatalysis, photocatalysis, and environmental remediation. High-entropy oxides (HEOs), an emerging class of HEAs with unique structures and tailorable properties, have gained significant attention from researchers due to their rainbow of versatile properties. HEOs possess some outstanding advantages, including excellent mechanical strength, high-temperature stability, stable material structure, and excellent magnetocaloric effect, and they are regarded as multifunctional in catalytic converters and thermoelectric, electromagnetic, energy, and data storage devices. The configurational entropy for HEOs is calculated from eqn (1):[15,16]

$$\Delta S_{\text{conf}} = -R\left[\left(\sum_{i=0}^{n} x_i \ \ln\ x_i\right)_{\text{cation-site}} + \left(\sum_{j=0}^{m} x_j \ \ln\ x_j\right)_{\text{anion-site}}\right], \quad (1)$$

where x_i represents the mole fraction of elements in the cation site, x_j represents the mole fraction of elements in the anion sites, and R is the general gas constant.[17]

In 2015, which is just a few years ago, the first HEO was reported by Rost *et al.*, which was composed of five metal atoms, [MgCoCuNiZn]O, a single-phase rock salt structure. The cation distribution was random and uniform in the crystal lattice.[18] Depending on the synthesis route and composition of HEOs, different crystal structures have been reported, including rock salt, fluorite type, perovskite, spinel and scheelite structures.[19–23] Various potential applications of HEOs in electrochemical technologies include Li-ion batteries, Zn–air batteries, electrocatalysis, supercapacitors, and solid oxide fuel cells. Oxygen evolution reaction (OER) and oxygen reduction reaction (ORR) are two main electrochemical reactions in various energy storage and conversion devices.

OER is a half reaction of electrochemical water splitting composed of four electron transfers. Because of its large overpotential and sluggish kinetics, OER requires a highly efficient, stable, and selective electrocatalyst to improve its kinetics.[24] State-of-the-art electrocatalysts (RuO_2/IrO_2) showed outstanding OER activity; however, their high cost, low availability, and weak stability hindered large-scale applications.[25] Transition metal-based materials, such as alloys, oxides, hydroxides, sulfides, phosphides, and nitrides, are emerging in the field of OER electrocatalysis because of their low cost, high abundance, and excellent stability in alkaline media.[26–29] HEOs are also potential catalysts for OER because the presence of multiple cations in the crystal structure provides a large number of active sites. Moreover, their high configurational entropy maintains their defect concentration (oxygen vacancies) and improves crystal stability, which leads to high activity.[30–33]

Huan He and coworkers synthesized $(FeCoNiCrMn)_3O_4$ spinel-type HEO coupled with a carbon sphere (CS) by applying the microwave solvothermal method and studied OER activity in alkaline media.[34] As-prepared HEO coupled CS demonstrated outstanding efficiency with a low overpotential of 263 mV at 10 mA cm^{-2}, a small Tafel slope of 41.24 mV dec^{-1} and long-term stability of 100 h. Wang *et al.* reported $(CoCuFeMnNi)_3O_4$ decorated with multi-walled carbon nanotubes prepared through low-temperature solvothermal technology. The prepared material showed the best OER performance with a low overpotential 350 mV at 10 mA cm^{-2} and a Tafel slope of 95.5 mV dec^{-1}.[35] Liu *et al.* explored the oxygen evolution reaction (OER) with $Mg_{0.2}Co_{0.2}Ni_{0.2}Cu_{0.2}Zn_{0.2}O$ electrocatalysts. HEO shows better intrinsic OER activities at 1.65 V compared to CoO and NiO, with turnover frequencies (TOFs) that are 15 and 84 times higher, respectively. Furthermore, chronopotentiometry testing at 10 mA cm^{-2} for over 25 hours showed only a minor decrease in the stability of HEO.[36] Zhang *et al.* prepared high entropy oxide $(CoNiMnZnFe)_3O_{3.2}$ using the mechanical alloying method, which exhibited a single-phase rock salt structure. Excellent OER performance was observed with an overpotential of 336 mV and a Tafel slope of 47.51 mV dec^{-1} at 10 mV cm^{-2}. This is because of the large number of MOOH nanosheets at the edge of the HEO core, which leads to a core–shell structure after electrochemical activation.[37] For instance, Duan *et al.* reported $(FeCoNiCrMn)_3O_4$, which exhibited a high catalytic activity towards OER with an overpotential of 288 mV at a current density of 10 mA cm^{-2} and outstanding stability (potential change of only 1.3% after a 95 h OER test at 10 mA cm^{-2}) in 1 M KOH electrolyte.[38] Lao and coworkers reported (CoNiCuZn)O doped with Fe, Mn, Mg and Al to form quinary HEO.[39] Among the different compositions of HEOs, (FeCoNiCuZn)O has demonstrated the best OER performance with an overpotential of 323 mV at a current density of 10 mA cm^{-2} and a Tafel slope of 64.5 mV dec^{-1} in 1 M KOH solution with a long-term stability of 50 h.[39] Several HEOs and HEAs with different elemental compositions and wt% have been reported to have outstanding OER activities.[40]

Herein, a series of equimolar (composed of 4, 5, and 6 metals) and non-equimolar with Al (25, 30, and 35%) HEOs are synthesized using the microwave irradiation method. The microwave irradiation method provides a time-saving and energy-saving strategy to control the precise composition, morphology, and structure of materials. After synthesis, the crystal structure, morphology, oxidation states, and chemical compositions of HEOs were studied using different analytical techniques. The OER activity of HEOs was studied in 1 M KOH and 1 M KOH + methanol at room temperature. Among equimolar HEOs, one with 5 metals (AlFeCuNiCo)O showed the best OER performance with a lower overpotential of 353 mV and Tafel slope of 52.3 mV dec^{-1} at a current density of 10 mA cm^{-2}. However, in non-equimolar HEOs, $Al_{0.3}[FeCuNiCo]_{0.7}O$ demonstrated low overpotential

(350 mV) and Tafel slope (49.4 mV dec^{-1}) at 10 mV s^{-1}. Other electrochemical parameters, including active surface area, double-layer capacitance, turnover frequency, and charge transfer resistance, were also calculated, which highlighted the best OER performance of all prepared HEO electrocatalysts. The prepared HEOs demonstrated long-term electrochemical stability for 3600 s.

2. Materials and methods

2.1. Materials

Aluminum nitrate nonahydrate ($Al(NO_3)_3{\cdot}9H_2O$, Sigma Aldrich, 99%), magnesium nitrate hexahydrate ($Mg(NO_3)_2{\cdot}6H_2O$, Sigma Aldrich, 99%), iron nitrate nonahydrate ($Fe(NO_3)_3{\cdot}9H_2O$, Sigma Aldrich, 99%), copper nitrate trihydrate ($Cu(NO_3)_2{\cdot}3H_2O$, Sigma Aldrich, 99%), nickel nitrate hexahydrate ($Ni(NO_3)_2{\cdot}6H_2O$, Sigma Aldrich, 99%), and cobalt nitrate hexahydrate ($Co(NO_3)_2{\cdot}6H_2O$, Sigma Aldrich, 99%) were used as metal precursors and employed as acquired without further purification. Ammonium hydroxide ($NH_4(OH)$, 3 M, Merck) was used to adjust the pH of the reaction medium.

2.2. Synthesis of high entropy oxides

The required stoichiometric amount of all metal precursors was taken and dissolved in deionized water using a magnetic stirrer at room temperature. After obtaining a homogeneous solution, the pH of the solution was adjusted to 12 with the addition of ammonium hydroxide in a controlled fashion. The gelatinous solution was further stirred for 30 minutes for complete homogenization. Then, the solution was exposed to microwave radiation for 3 minutes at 700 W heating power in a household microwave oven (frequency is ~2.45 GHz). The solution taken from the microwave was suddenly cooled in an ice bath. Next, the solution was centrifuged to separate the precipitated powder. Finally, the precipitated product was washed using deionized water and ethanol, and the washed samples were dried at 80 °C for 12 h in an oven. The dried sample was ground into a fine powder using a mortar and pestle and subjected to physical and chemical characterizations. The composition and sample codes of all prepared HEOs are listed in Table 1.

2.3. Material characterizations

2.3.1. Physical characterizations. X-ray diffraction (XRD) analysis was conducted to investigate the nature of the crystal structure and its associated properties using PANalytical Empyrean, CuK∞, λ = 1.5406 Å, and scan range: ($10^\circ \leq 2\theta \leq 90^\circ$) device with a step size of 0.02°. To determine the percentage of each metal in the complex system of as-synthesized high entropy oxides, an inductively coupled plasma-mass spectrometer (ICP-MS, Agilent 7800) was employed. To study the morphology of as-synthesized high entropy oxides, scanning electron microscopy (SEM) was used. Additionally, the elemental composition of the sample was determined by applying an energy dispersive X-ray spectrometer (EDS) performed during the SEM analysis. X-ray photoelectron spectroscopy (XPS, Specs-Flex XPS, energy range: 200 eV–4 keV) analysis was performed to study the oxidation states and electronic structure of the catalysts. The elemental composition and concentration of each metal in HEO were studied using energy dispersive X-ray spectroscopy.

Table 1 Composition of the synthesized high entropy oxides and their sample codes

	Composition	Sample code	Class
1	[AlFeCuNi]O	MEO-4	Medium entropy oxide
2	[AlFeCuNiCo]O	HEO-5	High entropy oxide
3	[AlMgFeCuNiCo]O	HEO-6	High entropy oxide
4	$Al_{0.25}[FeCuNiCo]_{0.75}O$	HEO-Al25	High entropy oxide
5	$Al_{0.30}[FeCuNiCo]_{0.70}O$	HEO-Al30	High entropy oxide
6	$Al_{0.35}[FeCuNiCo]_{0.65}O$	HEO-Al35	High entropy oxide

2.3.2. Electrochemical characterizations. Prepared high entropy oxides were tested as electrocatalysts for oxygen evolution reaction. Prior to the modification of the working electrode, its surface was polished with alumina slurry to remove any contamination on the electrode surface. For electrode modification, 5 μL ethanol was dropped on the electrode surface, followed by 0.1 mg of catalyst and 5 μL of Nafion solution. The modified electrode was dried at room temperature and employed for electrochemical studies. A conventional three-electrode system was used where Ag/AgCl (3 M KCl), modified glassy carbon (with a geometric area of 0.07 cm^2), and Pt wire were used as the reference, working, and counter electrodes, respectively. A Gamry Potentiostat 1010B electrochemical workstation was used for data acquisition.

1 M KOH was used as a supporting electrolyte, and a small amount of methanol was added to envision its effect on the kinetics of the OER process. Cyclic voltammetry was performed to investigate the OER activity of the prepared HEOs. For the electron transfer behavior and electrochemical stability of the designed electrocatalysts, EIS and chronoamperometry were employed, respectively. CV was also performed in non-faradaic regions to determine double-layer capacitance and electrochemical surface area. Prior to OER testing, the working electrode was activated electrochemically by cyclic voltammetry (CV) ranging from −1.5 to 1.5 V [*vs.* Ag/AgCl] at a scan rate of 100 mV s^{-1} for 50 cycles. In all electrochemical tests, the potential values obtained with respect to the Ag/AgCl reference electrode were converted into a reversible hydrogen electrode (RHE) using the following potential conversion formula:[41]

$$E_{RHE} = E_{Ag/AgCl} + 0.197 + 0.0591pH. \quad (2)$$

The OER onset and overpotential were examined by linear sweep voltammetry (LSV) at a current density of 10 mA cm^{-2} and a scan rate of 100 mV s^{-1} in both the KOH and KOH + methanol electrolytes. Tafel slopes (TS) are the thermodynamic scale for checking process feasibility, and they relate the kinetics of the electrochemical process to the inherent chemistries associated with the catalyst material. TS values for all electrocatalysts were obtained by plotting log (current density) *versus* the overpotential from the linear region of the LSV polarization curves and fitted into the Tafel equation:[42]

$$\eta = a + b\log j. \quad (3)$$

Active surface area (A) for all electrocatalyst-modified electrodes was determined through CV in the potential window of

0–0.6 V (*vs.* Ag/AgCl) using 1 M KCl + 5 mM potassium ferricyanide (redox couple). The Randles–Sevcik equation estimates the active surface area:[43]

$$I_p = 2.69 \times 10^5 n^{3/2} A C D^{1/2} \nu^{1/2}. \quad (4)$$

The electrochemical surface area (ECSA) correlates the surface properties of the catalytic materials with the feasibility of the process. To calculate the double layer capacitance (C_{dl}) and ECSA, CV experiments were performed in the non-faradaic region 0.3–0.7 V (*vs.* RHE) at scan rates of 20, 40, 60, 80, 100, 120, and 140 mV s^{-1}. Using the absolute values of the differences between the anodic and cathodic current densities at 0.55 V, a linear graph was obtained between the Δj ($j_{ox} - j_{red}$) and the scan rate, ν. C_{dl} was obtained from the slope of the linear plot, and ECSA was calculated using the following relation:[44]

$$\text{ECSA} = C_{dl}/C_s, \quad (5)$$

where C_s is the specific capacitance of the oxide smooth surface, which is typically 0.060 mF cm^{-2}.

Roughness factor (R_f) is another performance parameter for evaluating the catalytic nature of the envisioned materials. R_f of the modified electrodes was calculated by dividing the ECSA by the geometric area of the working electrode (0.07 cm^2). Higher ECSA and roughness factors are witnessed in the enhanced OER activity because many active sites are being exposed to electrochemical reactions.

Turnover frequency (TOF) is the direct estimate of the reaction kinetics. The TOF values were estimated by assuming that all metal atoms are involved in the electrochemical process. The following equation was used for the TOF calculations:[44]

$$\text{TOF} = j/4 \times F \times m, \quad (6)$$

where j is the current density at a specific overpotential, F is Faraday's constant, 4 is the total number of electrons involved in the OER process, and m is the number of moles of the catalyst used.

Electrochemical impedance spectroscopy (EIS) is a versatile technique used to endure a direct connection between the chemical nature of the catalyst material and the electrochemical stress (load). EIS analysis was conducted for all modified electrodes, and Nyquist plots were obtained at a frequency range of 0.1 Hz–20 kHz at the applied DC voltage in the range of 1.1–1.5 V. All the electrochemical experiments were carried out at room temperature.

3. Results and discussion

3.1. Physical characterization of prepared catalysts

The configurational entropy of all prepared HEOs was computed using eqn (1), where the anionic contribution was none because only oxygen was present at the anion site. Configurational entropy is dependent on the number of cations present in the composition and their wt% as well, regardless of their chemical nature, thus posing universality. The calculated configurational entropy for all prepared HEOs is summarized in Table 2.

Fig. 1(a) illustrates the XRD pattern of all prepared equimolar and non-equimolar high entropy oxides (HEOs). The diffraction peaks appearing at 2θ values around 36°, 42°, 62°, 74°, and 78° are highly consistent with the CoO diffraction peaks (PDF-# 78-0643 and PDF-# 43-1004) and can be indexed as (111), (200), (220), (311), and (222) planes of rock-salt crystal structure with space group $Fm\bar{3}m$, respectively.[36,39] No additional peak can be observed in the XRD pattern, which confirms the single-phase formation of the synthesized materials. All HEOs are monocrystalline without any phase segregation within the detection range. The relative intensities of the Bragg peaks (111) and (200) deviate from the ideal rock-salt lattice, revealing anisotropic strain broadening, as observed by Bérardan *et al.*[45] The average crystallite size, D_{av} for all prepared HEOs was calculated using the Debye–Scherrer equation, as illustrated in Table 2. The lowest D_{av} of 8.97 nm was estimated for HEO-Al30. This minimum crystallite size indicates better OER performance. ICP-MS analysis was carried out to determine the percentage of all constituents in the prepared HEOs, as summarized in Table 2. The wt% of metal constituents is similar to that of theoretical/stoichiometric amounts taken during synthesis.

Fig. 1(b)–(d) illustrates the SEM micrographs of HEO-5 at different magnification scales. At 10 μm, HEO-5 exhibited aggregates of nanoparticles with different shapes. However, high magnification (200 nm) particles have a spherical morphology. These spherical particles are almost similar in size and uniformly distributed throughout. SEM analysis confirmed the successful formation of HEOs using the microwave irradiation method with a controlled particle size.[46] The EDS spectrum of HEO-5 is shown in Fig. 1(e), which confirms the chemical composition, and all the metal atoms are present in equal or nearly equal concentrations. The EDS results (wt% and atomic%) of all the prepared samples are summarized in Table 3 and are in good agreement with the stoichiometric amounts used for synthesis.

XPS analysis was carried out to examine the elemental composition and oxidation states of the chemical constituents in the presence of HEOs. The XPS results of HEO-5 are shown in Fig. 2(b)–(g), which confirms the coexistence of all metal cations. Fig. 2(a) illustrates the core-level XPS spectra of Al 2p, Fe 2p, Cu 2p, Ni 2p, Co 2p, and O 1s acquired for the cations

Table 2 Average crystallite sizes, ICP-MS results (elemental wt%) and configurational entropy of all the prepared electrocatalysts

		Weight (wt%)						
Catalyst	D_{av} (nm)	Mg	Al	Fe	Co	Ni	Cu	ΔS_{config}
MEO-4	11.11		16.54	33.68		34.51	15.24	1.386R^a
HEO-6	9.62	8.58	11.64	23.60	26.20	20.28	9.66	1.791R
HEO-5	9.01		11.61	23.52	26.71	24.61	13.52	1.609R
HEO-Al25	12.43		14.70	21.87	24.82	23.74	14.84	1.602R
HEO-Al30	8.97		19.01	22.46	24.90	22.83	10.78	1.581R
HEO-Al35	9.17		22.15	20.71	23.24	22.20	11.67	1.548R

[a] It is medium entropy oxide by definition.

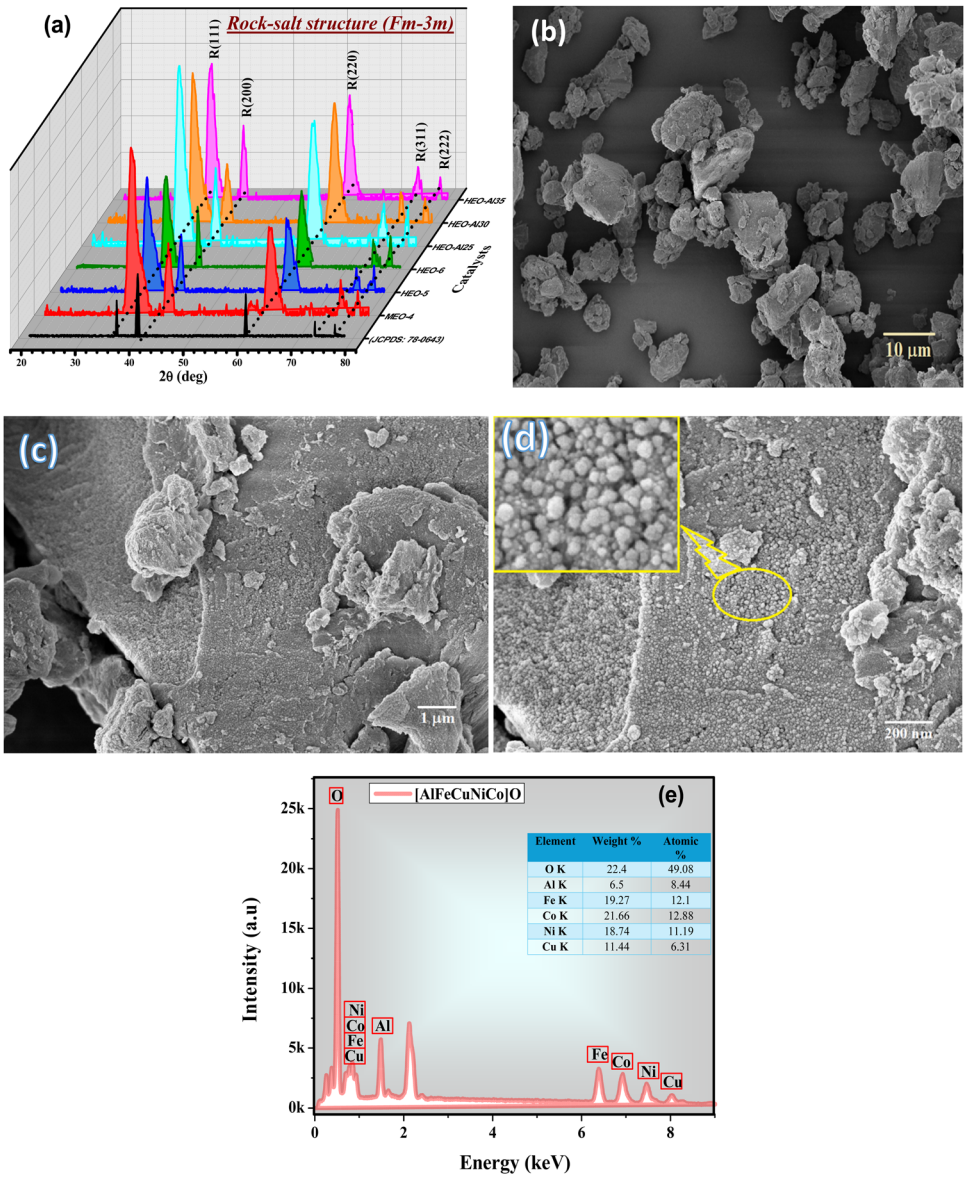

Fig. 1 Microstructure and chemical composition of the prepared HEO materials: (a) XRD patterns of all the prepared HEOs confirming the formation of a rocksalt-type crystal structure; (b)–(d) SEM images of HEO-5 at different magnifications, with the inset showing the spherical morphology of HEO-5; and (e) EDS analysis of HEO-5 with elemental percentages.

Table 3 Weight ratio and atomic ratio of all catalysts confirmed by EDS analysis

	EDS composition												
	Weight%							Atomic%					
Catalyst	O K	Mg K	Al K	Fe K	Cu K	Ni K	Co K	O K	Mg K	Al K	Fe K	Cu K	Ni K	Co K
MEO-4	28.37		10.39	26.82	11.9	22.51		55.25		12	14.97	5.84	11.95	
HEO-6	28.18	6.26	7.91	17.12	7.03	14.43	19.07	53.4	7.81	8.89	9.29	3.35	7.45	9.81
HEO-5	22.4		6.5	19.27	11.44	18.74	21.66	46.08		8.44	12.1	6.31	11.19	12.88
HEO-Al25	17.93		11.1	19.46	10.66	18.55	22.29	40.86		15.01	12.71	6.12	11.52	13.79
HEO-Al30	28.9		6.03	16.55	8.47	21.61	18.44	57.52		7.12	9.44	4.25	11.72	9.95
HEO-Al35	31.35		14.21	13.73	7.12	20.42	13.17	61.34		9.21	6.34	5.67	10.21	7.23

and anions of HEO-5. The spectral line for Al 2p is centered at 74.01 eV and 74.95 eV indexed to Al^{2+} and Al^{1+}, respectively.[41,47] In the Fe 2P spectra, spectral peaks centered at 712.2 eV and 725.3 eV represent $2P_{3/2}$ and $2P_{1/2}$ with their satellite peaks at

high energies. This spectrum also confirms the co-existence of Fe^{2+} and Fe^{3+} oxidation states.[39,42] Cu 2P spectra show $2P_{3/2}$ and $2P_{1/2}$ centered at 933.3 eV and 952.6 eV, respectively, with their corresponding satellite peaks. The peak at $2P_{3/2}$ confirms the

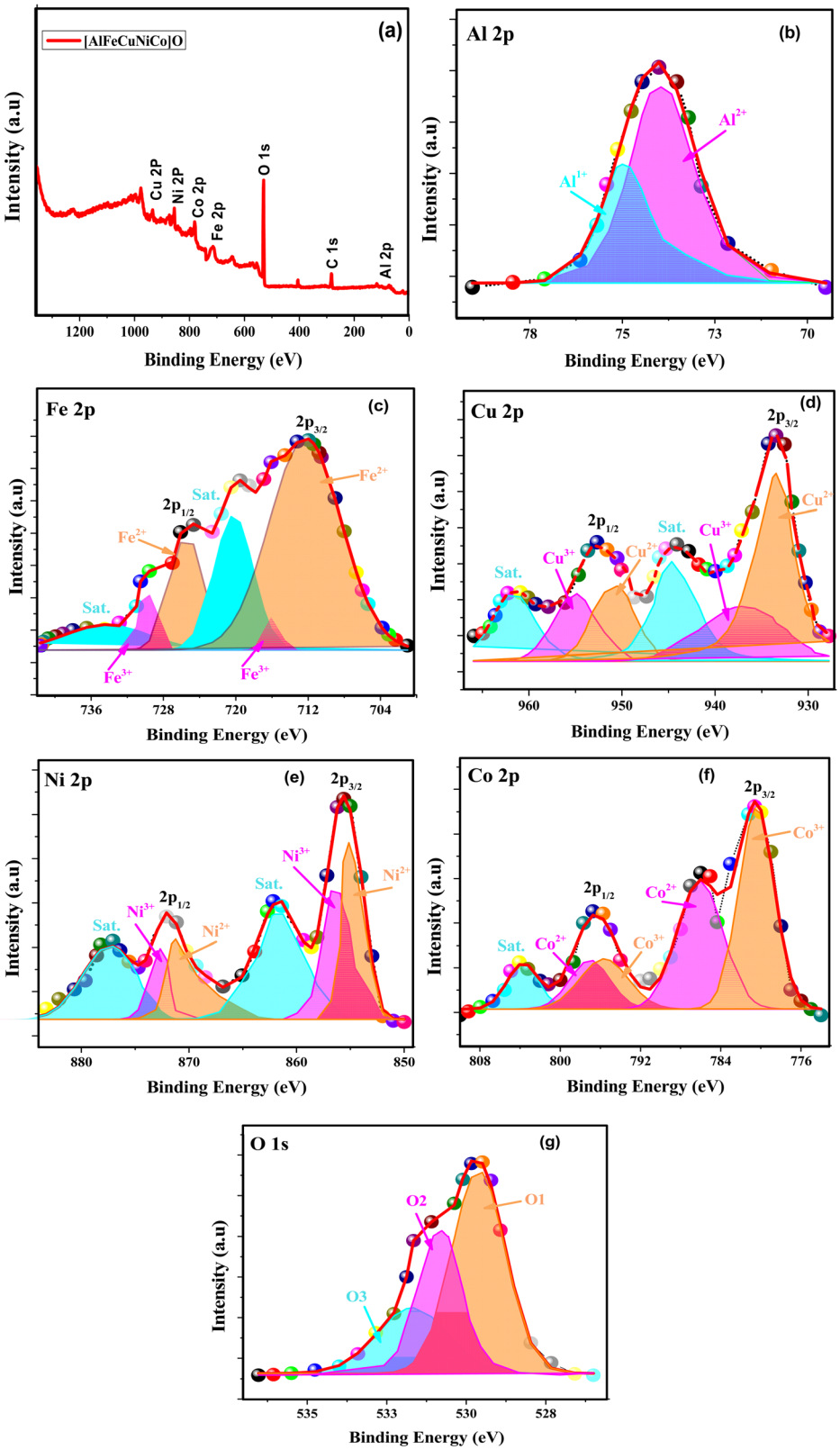

Fig. 2 (a) XPS full range spectra of HEO-5 and (b)–(g) XPS high-resolution spectrum of Al, Fe, Cu, Ni, Co, and O of HEO-5 composition.

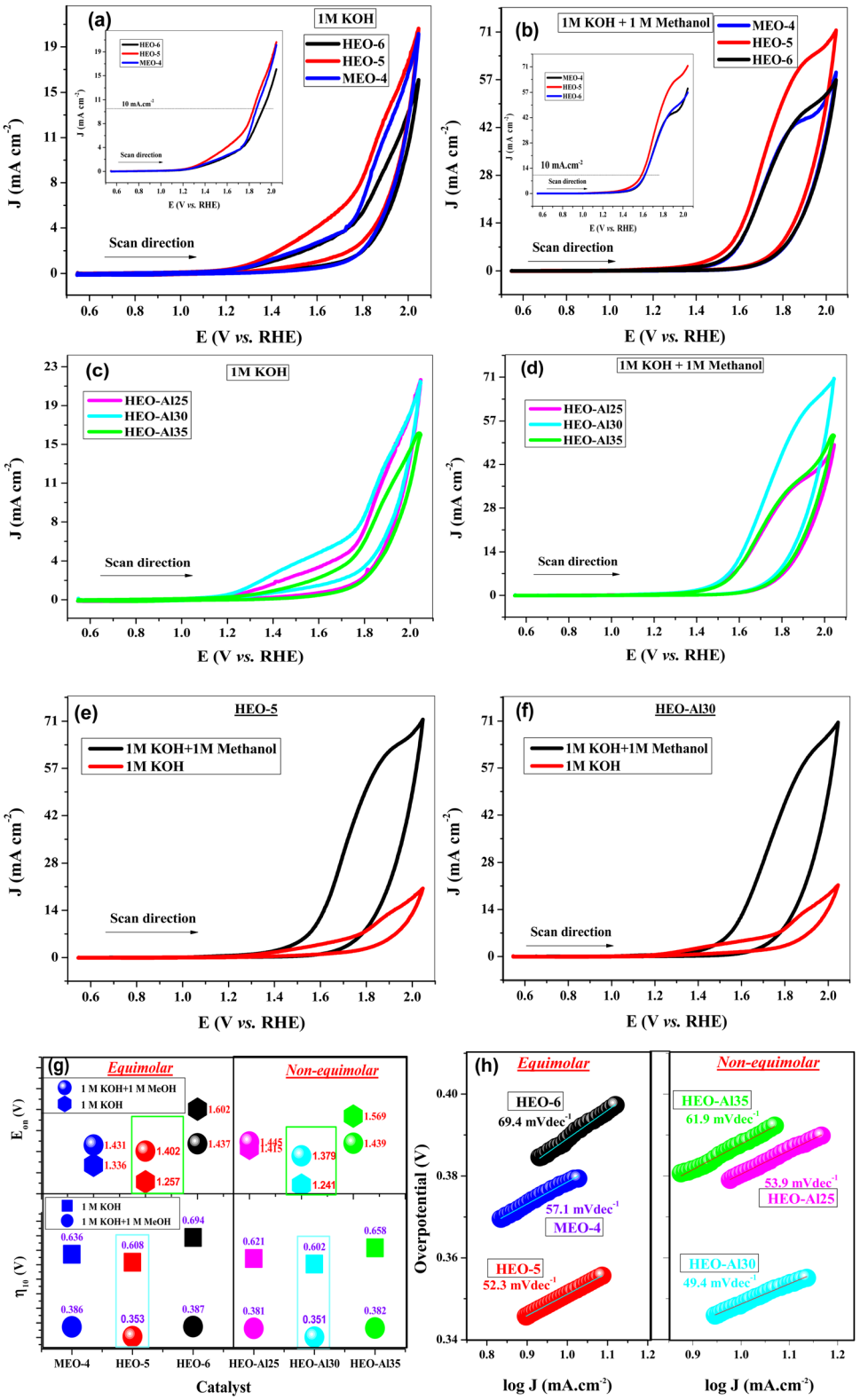

Fig. 3 Cyclic voltammograms of equimolar HEOs (MEO-4, HEO-5, and HEO-6) in (a) 1 M KOH and (b) 1 M KOH + 1 M methanol. Inset shows the LSV response of the same catalyst. (c) and (d) Cyclic voltammograms of non-equimolar HEOs (HEO-Al25, HEO-Al30, and HEO-Al35) in 1 M KOH and 1 M KOH + 1 M methanol. LSV scans are shown in figure inset, (e) and (f) CV responses of HEO-5 and HEO-Al30 in the absence (red) and presence (black) of methanol, (g) onset and overpotential of all HEOs in 1 M KOH and 1 M KOH + 1 M methanol recorded at 10 mA cm^{-2} current density, and (h) Tafel slopes of all the prepared HEOs calculated in 1 M KOH +1 M methanol.

presence of Cu^{2+}/Cu^{3+}; however, the ratio of Cu^{2+} is more than 70%, which confirms that Cu^{2+} is present throughout the samples.[48] Ni 2P spectra also exhibit $2P_{3/2}$ and $2P_{1/2}$ at 855.7 eV and 871.8 eV, respectively. Satellite peaks at higher energies are also observed in the spectra. The $2P_{3/2}$ appearing at 853.7–855.7 eV, and the $2P_{1/2}$ appearing at 870.5 eV–872.1 eV confirmed the presence of Ni^{2+} oxidation state.[14,49] In CO 2P spectra, peaks centered at 780.4 eV and 796.3 eV correspond to $2P_{3/2}$ and $2P_{1/2}$, respectively, with their satellite peaks. Peaks at 779.2 eV–781.9 eV for $2P_{3/2}$ confirmed the presence of Co^{2+} oxidation states.[34,44,50] The XPS spectra confirmed that all metal cations are present as divalent corresponding to the rock-salt crystal structure. Fig. 2(g) depicts the XPS spectra of O 1s, consisting of one intense and two shoulder peaks. These three peaks appeared at 529.7 eV, 530.8 eV, and 531.9 eV, which correspond to the lattice oxygen (O1), metal oxide oxygen vacancy (O2), and surface-adsorbed oxygen (O3), respectively. Oxygen vacancy contribution is significant in spectra, suggesting that HEOs are rich in oxygen vacancies.[51–53] Energy storage characteristics are significantly influenced by oxygen vacancies because they enhance electrical conductivity by increasing the concentration of charge carriers. Oxygen vacancies can also accelerate overall surface kinetics, promote OH adsorption, and act as an electroactive center for redox processes. Consequently, oxygen vacancies enhance specific capacitance and electrical conductivity and serve as an electroactive core for the ultrafast surface redox reaction.[54]

3.2. OER performance of prepared electrocatalysts

The electrochemical measurements were carried out to investigate the OER performance of all equimolar and non-equimolar HEOs in alkaline media (1 M KOH and 1 M KOH + methanol) using a conventional three-electrode setup. CV and LSV experiments were performed to record the OER responses of the HEO-modified electrodes. Comparative CV and LSV voltammograms of equimolar HEOs in 1 M KOH and 1 M KOH + 1 M methanol are shown in Fig. 3(a) and (b), respectively. Among the three equimolar compositions, HEO-5 demonstrated the best OER performance, which was attributed to the high configurational entropy and large number of active sites present on the surface of the catalyst. The decrease in the OER activity of HEO-6 is due to the presence of Mg, which may hinder some active sites and create a deactivation layer at the surface.[55] A higher ionic radius of Mg ions hinders the formation of oxygen vacancies on the catalyst surface, which are crucial for the adsorption and activation of water molecules. Additionally, the strong affinity of Mg for oxygen leads to the formation of the Mg–O bond, which competes with the formation of THE O–O bond necessary for the OER, hence decreasing the overall efficiency of the catalyst. The OER responses of non-equimolar HEOs recorded in 1 M KOH and 1 M KOH + 1 M methanol are shown in Fig. 3(c) and (d), respectively. HEO-Al30 exhibited the best OER response with a high output current and low overpotential. The addition of methanol increases the OER response, which is due to an increase in hydroxyl ions in the electrolyte (directly related to oxygen production) and a decrease in the hindrance of the conversion of hydroxyl ions to oxygen molecules. Furthermore, a salt-like specie ($CH_3O^-\cdots K^+$) was produced upon the addition of methanol in KOH, which increased the adsorption of OH^- ions on the surface of catalysts; therefore, enhanced OER response was observed.[43,56,57] Methanol oxidation reaction (MOR) requires lower potential (0.016 V *vs.* RHE) compared to OER and occurs during the OER study. MOR requires high overpotential, has slower kinetics than OER and produces less current (in μA). However, when we scan the potential limit to a higher value for OER, the anodic peak observed for MOR diminishes because of the high current obtained for the OER process (in mA). Methanol-assisted HER and OER have been reported over various catalysts, emphasizing the positive effect of the addition of methanol during water splitting analysis.[58] Comparative cyclic voltammograms of HEO-5 and HEO-Al30 are shown in Fig. 3(e) and (f), which clearly show that there is a pronounced increase in the OER output current upon the addition of methanol. The CV responses of the other prepared samples are summarized in Fig. S1 (ESI†).

The onset potential E_{on} is an important parameter used for the evaluation of the electrocatalyst activity of material.[59] For all HEO-modified electrodes, E_{on} was calculated in both media, *i.e.*, KOH and KOH + methanol. The minimum onset potentials were observed for HEO-5 (1.257 V and 1.402 V) and HEO-Al30 (1.241 V and 1.379 V) in 1 M KOH and 1 M KOH + 1 M methanol, respectively. The calculated onset potential values for all HEO-modified electrodes in 1 M KOH and 1 M KOH + 1 M methanol are shown in Fig. 3(g). These low onset potential values of HEOs make them potential candidates for future electrocatalysis technologies. Another important parameter for measuring catalytic efficiency is the overpotential value, which reflects the improvement in the kinetics of the OER process. The main purpose of catalyst development is to decrease the overpotential barrier associated with the four-electron transfer of the OER process.[60] The overpotential values for all modified electrodes were calculated at a 10 mA cm^{-2} current density in 1 M KOH and 1 M KOH + 1 M methanol. Minimum overpotential was observed for HEO-5 in equimolar compositions, which were 353 mV (in 1 M KOH + 1 M methanol) and 608 mV (in 1 M KOH). However, in non-equimolar compositions, HEO-Al30 possessed minimum overpotential values of 350 mV (in 1 M KOH + 1 M methanol) and 602 mV (in 1 M KOH). The overpotential values for all HEOs in both mediums are shown in Fig. 3(g). The low overpotential values suggest that HEOs accelerate the OER electrocatalysis more efficiently.

The Tafel slope is an important parameter in describing the catalytic activity, kinetics, and mechanism of OER electrocatalysis. The smaller value of the Tafel slope reflects the faster OER kinetics.[60] Fig. 3(h) shows the Tafel slopes of all equimolar and non-equimolar HEOs calculated at a 10 mA cm^{-2} current density. The minimum Tafel slopes were 52.3 mV dec^{-1} and 49.4 mV dec^{-1} for HEO-5 and HEO-Al30, respectively. This suggests that the rate determining step of the OER occurs in the middle or at the end of the multiple electron transfer reaction.

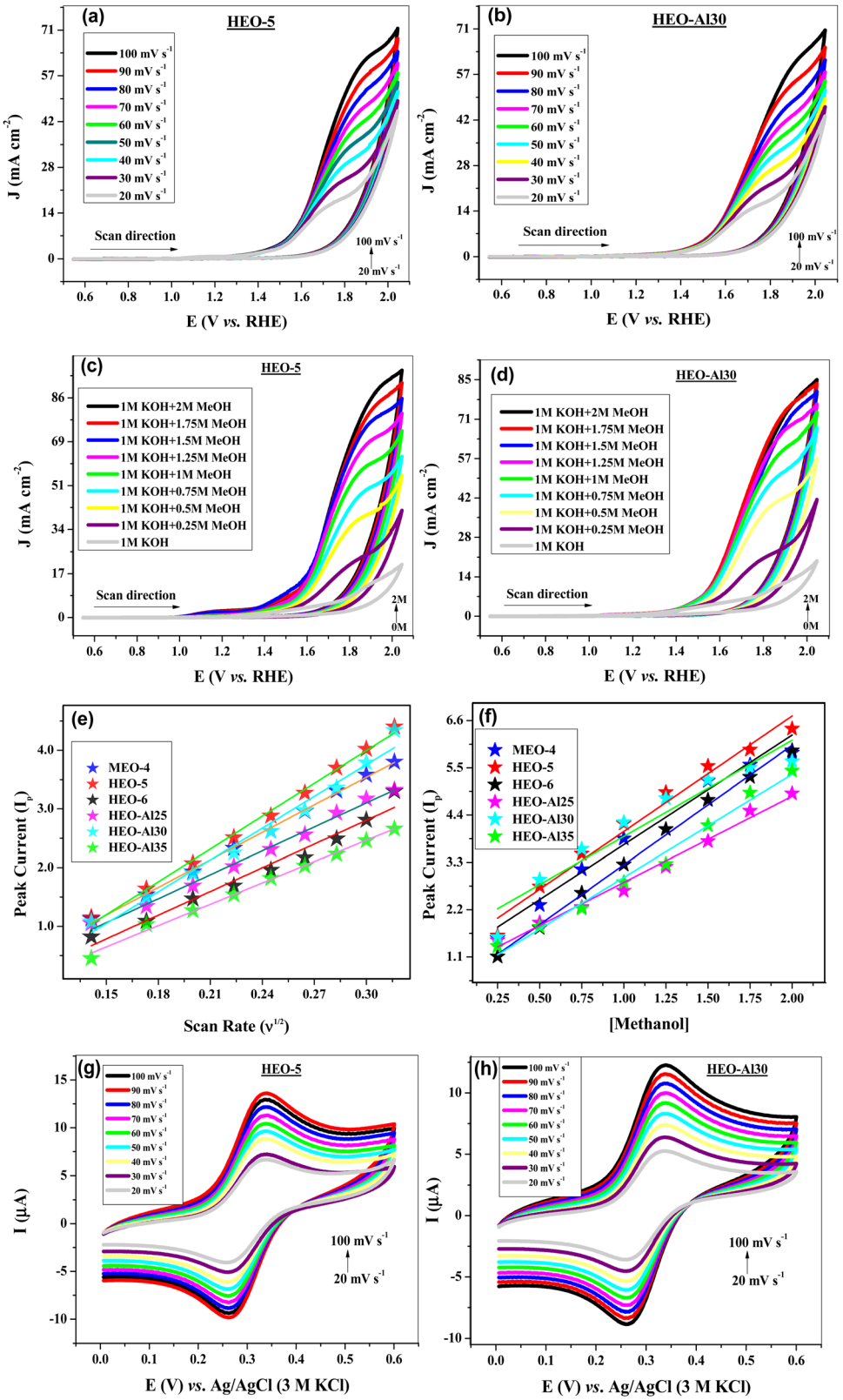

Fig. 4 Cyclic voltammograms of (a) HEO-5 and (b) HEO-Al30 in 1 M KOH + 1 M methanol at 20–100 mV s^{-1} scan rate. (c) and (d) OER response of HEO-5 and HEO-Al30 at 100 mV s^{-1} in 0-2 M methanol, (e) linear plots of peak current *versus* scan rate for all the HEO-modified electrodes, (f) dependence of peak current on methanol concentrations for all the HEO-modified electrodes, and (g), (h) CV response of HEO-5 and HEO-Al30 in 1 M KCl + 5 mM potassium ferricyanide redox couple at a 20–100 mV s^{-1} scan rate.

The diffusion coefficient is another parameter used to determine the electrocatalytic activity of any material. This tells us how rapidly the analyte species diffuse towards the electrode surface. To determine the diffusion coefficients for all HEO electrocatalysts, cyclic voltammograms were recorded in 1 M KOH + 1 M methanol at scan rates ranging from 20 to 100 mV s^{-1}. Fig. 4(a) and (b) illustrate a record of the OER responses of HEO-5 and HEO-Al30, respectively, where the peak current increased with increasing scan rate by verifying the diffusion-controlled mechanism of the OER process. Linear graphs of I_p *vs.* $\nu^{1/2}$ were plotted, as shown in Fig. 4(e), and from the slope values, the diffusion coefficients for all HEOs were calculated using the Randles Sevcik equation, as summarized in Table 4. The mass transport coefficients for all prepared high entropy materials were also calculated, as summarized in Table 4. The highest values of diffusion coefficients (2.2×10^{-8} cm^2 s^{-1} and 1.9×10^{-8} cm^2 s^{-1}) and mass transport coefficients (2.9×10^{-4} cm s^{-1} and 2.7×10^{-4} cm s^{-1}) were obtained for HEO-5 and HEO-Al30, respectively.

The effect of methanol addition in the electrolyte on the OER response of all HEO-modified electrodes was also investigated. The OER kinetics improved efficiently at the initial steps and gradually at later steps as the methanol concentration increased (0–2 M). Fig. 4(c) and (d) show the voltammograms of HEO-5 and HEO-Al30 at varying methanol concentrations, where the peak current increases with methanol concentration. Heterogenous rate constant k°, which informs us of the reaction kinetics of the OER process occurring at the electrode–electrolyte interface, is also an important parameter for evaluating electrocatalytic activity.[61,62] Linear graphs of I_p *vs.* [methanol] were plotted, as shown in Fig. 4(f). From the slope values, k° was calculated for the HEO-modified electrode using the Reinmuth equation. Better k° values of 5.85×10^{-4} cm s^{-1} and 5.51×10^{-4} cm s^{-1} were obtained for HEO-5 and HEO-Al30, respectively.

The redox behavior of the HEO-modified electrode was investigated through cyclic voltammetry using 1 M KCl + 5 mM potassium ferricyanide redox couple in the potential range of 0–0.6 V [*vs.* Ag/AgCl] at 20–100 mV s^{-1} sweep rates. The CV voltammograms of HEO-5 and HEO-Al30 are shown in Fig. 4(g) and 3(h), respectively, which confirm one electron transfer process, and the peak current increases linearly with the scan rate. The CV responses of the other materials are shown in Fig. S2 (ESI†). The active surface area for all HEO-modified electrons was calculated from the observed peak current value using the Randles Sevcik equation.[63] For different HEO compositions, active surface area (A) was observed in the range of 0.0065–0.0116 cm^2, where the highest value was observed for the HEO-5-modified electrode. The calculated active surface area for all compositions is shown in Fig. 5(a).

Another critical parameter frequently used for the evaluation of catalytic activity is electrochemical active surface area (ECSA), which can be determined from double-layer capacitance (C_{dl}). CV was performed in the non-faradaic region (0.32–0.72 V *vs.* RHE). Fig. 5(b) and (c) show the cyclic voltammograms of HEO-5 and HEO-Al30 at a scan rate of 20–160 mV s^{-1}, respectively. Linear plots were drawn between Δj (difference of anodic and cathodic current densities at 0.55 V) as a function of scan rate for all prepared HEOs electrocatalysts, as shown in Fig. 4(d). Compared to other catalysts, HEO-Al35 exhibits a superior double-layer capacitor and maximum ECSA value (7.503 cm^2), which is significantly larger than the values for MEO-4 (7.208 cm^2), HEO-5 (4.721 cm^2), HEO-6 (2.461 cm^2), HEO-Al25 (2.146 cm^2), and HEO-Al30 (5.601 cm^2). It can be observed that increasing the optimum concentration of a specific metal constituent leads to exposure to more active sites.[64] Estimated C_{dl}, ECSA, and R_F for all HEOs are summarized in Table 5.

TOF values were calculated using eqn (6) by assuming a hundred percent faradaic efficiency at 500 mV overpotential in 1 M KOH and 1 M KOH + 1 M methanol, as shown in Fig. 5(e). Among equimolar compositions, the highest value of TOF was obtained for HEO-5 (0.221 s^{-1} in 1 M KOH and 1.388 s^{-1} in 1 M KOH + 1 M methanol), whereas for MEO-4 (0.144 s^{-1} and 1.047 s^{-1}) and HEO-6 (0.138 s^{-1} and 1.026 s^{-1}) values were obtained in 1 M KOH and 1 M KOH + 1 M methanol, respectively. In the case of non-equimolar HEOs, HEO-Al30 possessed high TOF values of 0.228 s^{-1} and 1.252 s^{-1} in 1 M KOH and 1 M KOH + 1 M methanol, respectively. To investigate the long-term electrochemical stability of the prepared HEO electrocatalysts, chronoamperometric analysis was carried out for 3600 s. The responses of all electrocatalysts are shown in Fig. 5(f) over the entire investigation period. For the first 800 s, the responses were irregular due to the activation of surface particles; however, after the activation, all the HEO-modified electrodes showed outstanding stability with a negligible decrease in output current.[65] For a longer time stability test, HEO-5 was selected, and chronoamperometric analysis was carried out for 4 h. The catalyst was stable over the entire duration, and the same output current was obtained, confirming the physical and electrochemical stability of the catalyst surface at the electrode/electrolyte interface. The stability test response of HEO-5 is shown in Fig. S4 (ESI†).

Table 4 Electrocatalytic parameters of all the prepared HEOs derived from OER response

Catalyst	Diffusion coefficient, $D^\circ/ \times 10^{-8}$ (cm^2 s^{-1})	Mass transport coefficient, $m_T/ \times 10^{-4}$ (cm s^{-1})	Heterogeneous rate constant, $k^\circ/ \times 10^{-4}$ (cm s^{-1})	α	Over-potential η_{10} (mV)	Tafel slope (mV dec^{-1})
MEO-4	1.8	2.6	5.44	0.934	386	57.1
HEO-5	2.2	2.9	5.85	0.943	353	52.3
HEO-6	1.1	2.0	5.01	0.941	387	69.4
HEO-Al25	1.4.	2.3	4.17	0.938	380	53.9
HEO-Al30	1.9	2.7	5.51	0.942	350	49.4
HEO-Al35	0.8	1.7	4.49	0.932	381	61.9

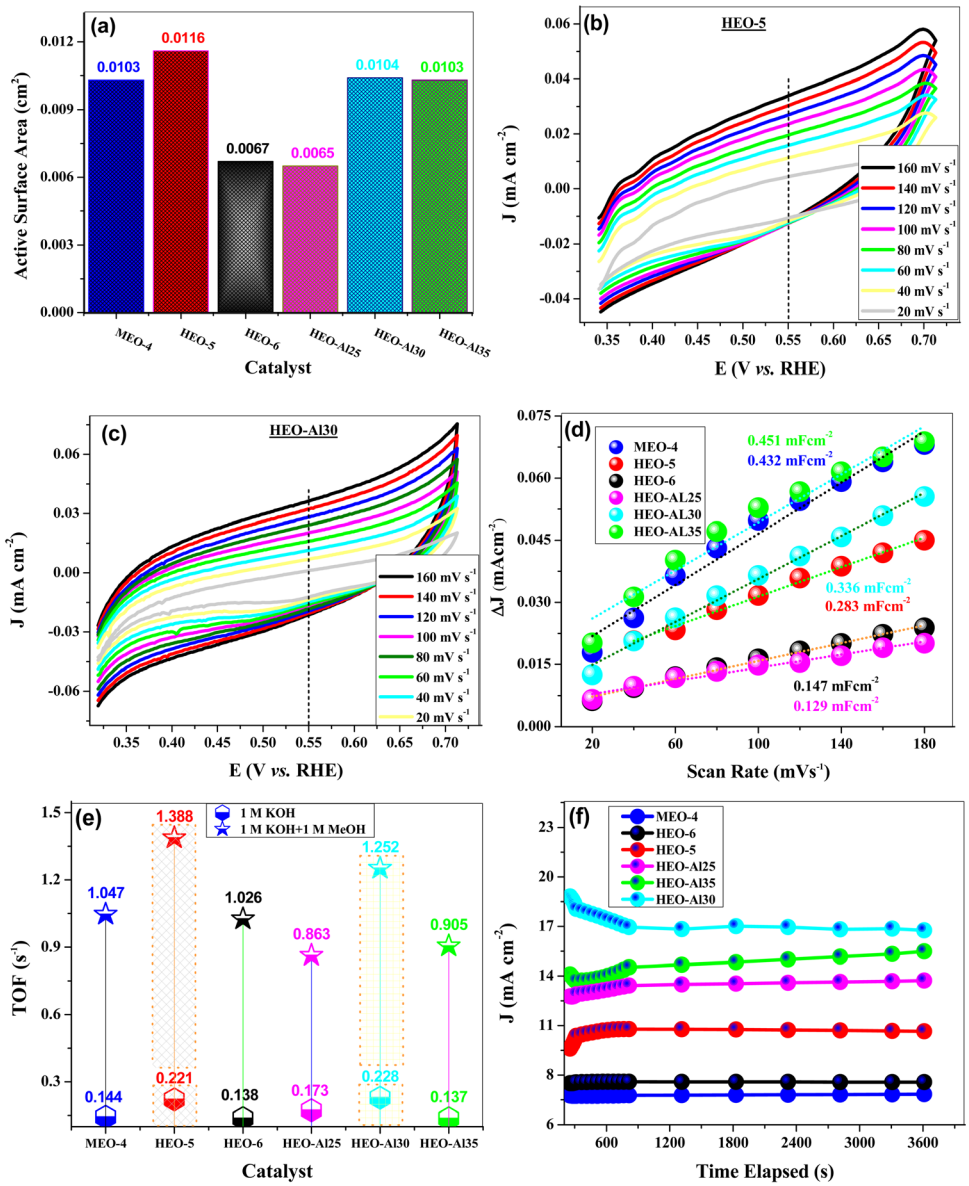

Fig. 5 (a) Bar graphs showing active surface area of all the prepared HEOs, (b) and (c) CV response of HEO-5 and HEO-Al30 in the non-faradaic region at a 20–160 mV s^{-1} scan rate, (d) linear plots of all the HEO-modified electrodes for double layer capacitance calculation, (e) turnover frequency values of all the prepared HEOs in 1 M KOH and 1 M KOH + 1 M methanol, and (f) chronoamperometric responses of all the HEO-modified electrodes at 1.4 V for 3600 s.

To reveal the OER kinetics of all prepared HEOs, electrochemical impedance spectroscopy (EIS) was performed in 1 M KOH and 1 M KOH + 1 M methanol at different applied potentials. EIS parameters calculated from the equivalent circuit model fitting of Nyquist plots are summarized in Table 6, where HEO-5 and HEO-Al30 showed lower impedance values.

Table 5 Active surface area, C_{dl}, ECSA and TOF values of all the HEO materials retrieved from cyclic voltammograms

Catalyst	Active surface area A (cm^2)	Double layer capacitance C_{dl} (mF cm^{-2})	Electro-chemical surface area ECSA (cm^2)	Roughness factor R_f	Turnover frequency TOF (s^{-1})	
					1 M KOH	1 M KOH + 1 M methanol
MEO-4	0.0103	0.4325	7.208	102.97	0.144	1.047
HEO-5	0.0116	0.2833	4.721	67.44	0.221	1.388
HEO-6	0.0067	0.1477	2.461	35.15	0.138	1.026
HEO-Al25	0.0065	0.1288	2.146	30.65	0.173	0.863
HEO-Al30	0.0104	0.3361	5.601	80.01	0.228	1.252
HEO-Al35	0.0103	0.4502	7.503	107.18	0.137	0.905

Table 6 Electrocatalytic parameters retrieved from the equivalent circuit model fitting of EIS analysis

	1 M KOH				1 M KOH + 1 M methanol			
Catalyst	R_s (Ω)	R_{ct} (Ω)	CPE (μF)	α	R_s (Ω)	R_{ct} (Ω)	CPE (μF)	α
MEO-4	34.94	97.25	2.53	0.90	25.01	30.02	6.70	0.83
HEO-5	26.12	93.61	7.77	0.91	28.90	35.67	5.45	0.91
HEO-6	65.78	145.41	8.17	0.80	30.02	46.01	7.90	0.79
HEO-Al25	30.83	75.21	7.67	0.81	33.03	50.05	7.76	0.81
HEO-Al30	26.01	68.81	8.79	0.93	27.01	35.03	6.84	0.84
HEO-Al35	33.34	97.82	6.93	0.82	39.04	64.02	6.86	0.86

Fig. 6(a) shows the Nyquist plots of HEO-5 in 1 M KOH and 1 M KOH + 1 M methanol, which signifies that the addition of methanol decreases the charge transfer resistance by decreasing the diameter of the semicircle. These results agree well with the CV response in the presence and absence of methanol. Nyquist plots were also recorded at different DC voltages (1.1–1.5 V), as shown in Fig. 6(b). Charge transfer resistance R_{ct} decreases with increasing applied potential due to a decrease in

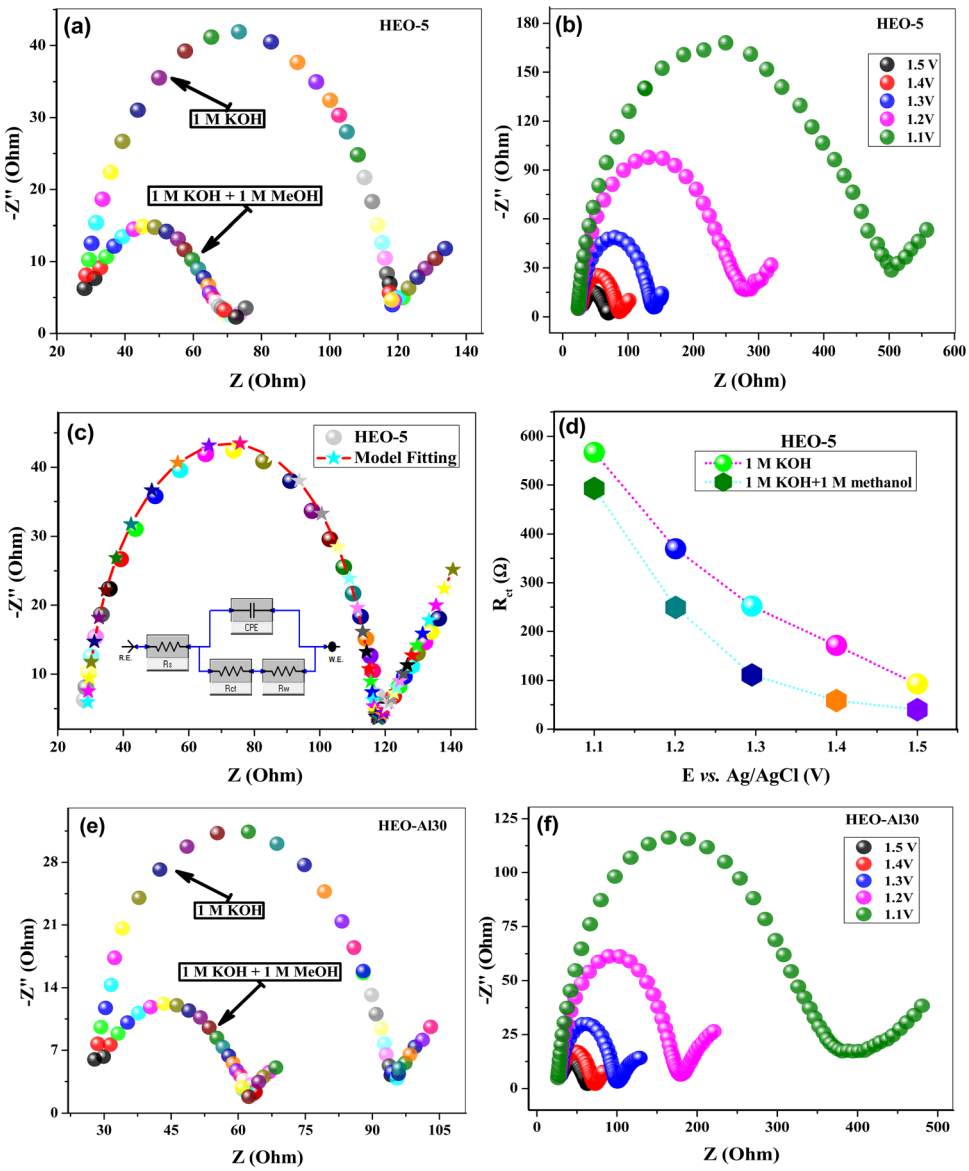

Fig. 6 (a) Nyquist plots of the HEO-5-modified electrode in the 1 M KOH and 1 M KOH + 1 M methanol, (b) Nyquist plots of the HEO-5 modified electrode at 1.1–1.5 V applied DC voltage, (c) Nyquist plot of HEO-5 with equivalent circuit model fitting and the circuit diagram, (d) R_{ct} values of HEO-5 in 1 M KOH and 1 M KOH + 1 M methanol at different DC voltages, (e) Nyquist plots of the HEO-Al30-modified electrode in 1 M KOH and 1 M KOH + 1 M methanol, and (f) Nyquist plots of the HEO-Al30-modified electrode at 1.1–1.5 V applied DC voltage.

the overpotential barrier for the electron transfer process occurring at the electrode/electrolyte interface. Fig. 6(c) shows the equivalent circuit model fitting of the Nyquist plots and the resultant equivalent circuit model used for the calculation of EIS parameters.[64,66] R_{ct} values of HEO-5 recorded in 1 M KOH and 1 M KOH + 1 M methanol at different applied DC voltages are shown in Fig. 6(d). All HEOs presented similar responses during The EIS analysis, where Fig. 6(e) and (f) show Nyquist plots of HEO-Al30 in different electrolytes and at different applied potentials, respectively. EIS Nyquist plots of other materials at different applied voltages are shown in Fig. S3 (ESI†). The overall outstanding OER activity of HEO-Al30 is attributed to the optimum concentration of Al within the HEO composition. Because of the smaller cationic size of Al and its potential to form an Al–O bond, HEO-Al30 showed high electrical conductivity and a large number of surface sites to adsorb water molecules. Furthermore, Al incorporation alters the electronic structure of HEOs and improves synergy within the crystal structure, leading to the formation of oxygen vacancies. Peng yang *et al.* reported Al-based HEO and HEF that showed better OER performance and required 293 mV and 261 mV overpotential at a 10 mA cm^{-2} current density.[67]

4. Conclusions

In summary, high-entropy oxide-structured catalysts were synthesized successfully using the easy and rapid microwave technique. The physical characterization results of the synthesized catalysts indicated that structures with the desired metal ratios were successfully achieved. The OER performances of the catalysts were assessed in an alkaline electrolyte. Based on the studies of CV, LSV, and chronoamperometry, it was found that the $Al_{0.3}(FeCuNiCo)_{0.7}O$ (HEO-Al30) catalyst had an overpotential of 350 mV and a Tafel slope value of 49.4 mV dec^{-1} at a current density of 10 mA cm^{-2} and exhibited better OER performance attributed to high configurational entropy (1.581*R*) and optimum concentration of Al (30%). EIS conducted under different electrolyte conditions demonstrates that the HEO-Al30 catalyst is the optimal catalyst for the OER. The enhanced activity of the HEO-Al30 catalyst can be attributed to the synergistic effect resulting from the interaction between the metals present in its structure. Moreover, the results indicate that the proportion of metal composition in the catalyst structure has a substantial impact on the OER activity. Therefore, we can conclude that the abundance of cations and anions in the structure leads to a reorganization of the electronic structure, resulting in enhanced OER activity. Based on the findings of this study, we believe that high-entropy oxide structures can pioneer the development of new catalysts that are highly active in OER and cheap by controlling the ratio of elements.

Author contributions

Muhammad Asim, Akbar Hussain, Sadia Kanwal, Yasemin Aykut: conceptualization, methodology, investigation, writing – original draft, writing – review & editing, visualization. Awais Ahmad, Ayşe Bayrakçeken: conceptualization, co-supervision, writing – review & editing, Mmterial characterizations. Naveed Kausar Janjua: principal supervisor. All authors have read and agreed to the published version of the manuscript.

Data availability

The data that support the plots in this paper and other findings of this study are available from the corresponding author upon reasonable request.

Conflicts of interest

There are no conflicts to declare.

Acknowledgements

Muhammad Asim and Akbar Hussain greatly acknowledge Türkiye Burslari Scholarship for financial assistance and Atatürk University East Anatolia High Technology Application and Research Center (DAYTAM) for providing material characterizations.

References

1 M. Anandkumar and E. Trofimov, *J. Alloys Compd.*, 2023, 170690.
2 K. Kusada, M. Mukoyoshi, D. Wu and H. Kitagawa, *Angew. Chem., Int. Ed.*, 2022, **134**, e202209616.
3 Y. Pan, J.-X. Liu, T.-Z. Tu, W. Wang and G.-J. Zhang, *Chem. Eng. J.*, 2023, **451**, 138659.
4 J. W. Sturman, E. A. Baranova and Y. Abu-Lebdeh, *Front. Energy Res.*, 2022, **10**, 862551.
5 Y. Ma, Y. Ma, Q. Wang, S. Schweidler, M. Botros, T. Fu, H. Hahn, T. Brezesinski and B. Breitung, *Energy Environ. Sci.*, 2021, **14**, 2883–2905.
6 J. W. Yeh, S. K. Chen, S. J. Lin, J. Y. Gan, T. S. Chin, T. T. Shun, C. H. Tsau and S. Y. Chang, *Adv. Eng. Mater.*, 2004, **6**, 299–303.
7 B. Cantor, I. Chang, P. Knight and A. Vincent, *Mater. Sci. Eng., A*, 2004, **375**, 213–218.
8 A. Amiri and R. Shahbazian-Yassar, *J. Mater. Chem. A*, 2021, **9**, 782–823.
9 Y. Wang, *Adv. Appl. Ceram.*, 2022, **121**, 57–78.
10 S. Li, L. Tong, Z. Peng, B. Zhang and X. Fu, *Green Chem.*, 2024, **26**, 384–395.
11 X. Wang, Z. Zhan, H. Cao and Y. Zhang, *Ceram. Int.*, 2024, DOI: **10.1016/j.ceramint.2024.01.409**.
12 J. Li, S. Chen, H. Fan, Q. Zhang, Y. Su, J. Song, L. Hu, Y. Zhou and Y. Zhang, *J. Am. Ceram. Soc.*, 2024, **107**, 2750–2764.
13 Z. Tang, Z. Wen, Y. Liu, L. Zhuang, H. Yu and Y. Chu, *Adv. Funct. Mater.*, 2024, **34**, 2312239.
14 D. Wang, C. Duan, H. He, Z. Wang, R. Zheng, H. Sun, Y. Liu and C. Liu, *J. Colloid Interface Sci.*, 2023, **646**, 89–97.

15 B. L. Musicó, D. Gilbert, T. Z. Ward, K. Page, E. George, J. Yan, D. Mandrus and V. Keppens, *APL Mater.*, 2020, **8**, 040912.
16 S. Schweidler, M. Botros, F. Strauss, Q. Wang, Y. Ma, L. Velasco, G. Cadilha Marques, A. Sarkar, C. Kübel and H. Hahn, *Nat. Rev. Mater.*, 2024, 1–16.
17 A. Sarkar, L. Velasco, D. Wang, Q. Wang, G. Talasila, L. de Biasi, C. Kübel, T. Brezesinski, S. S. Bhattacharya and H. Hahn, *Nat. Commun.*, 2018, **9**, 3400.
18 C. M. Rost, E. Sachet, T. Borman, A. Moballegh, E. C. Dickey, D. Hou, J. L. Jones, S. Curtarolo and J.-P. Maria, *Nat. Commun.*, 2015, **6**, 8485.
19 J. R. Santos, R. A. Raimundo, F. d. A. João, J. d. S. Hortencio, F. J. Loureiro, D. A. Macedo, M. A. Morales, I. Gualandi, D. Tonelli and U. U. Gomes, *J. Electroanal. Chem.*, 2024, 118191.
20 X. Ping, Q. Yang, B. Meng, Z. Ma and X. Pan, *J. Alloys Compd.*, 2024, **975**, 172971.
21 X. Ji, F. Yang, Y. Du, J. Li, J. Li and Q. Hu, *J. Mater. Sci. Technol.*, 2024, **168**, 71–78.
22 A. K. Gupta, A. Singh, P. Kumari, N. K. Giri and R. R. Shahi, *Energy Storage*, 2024, **6**, e538.
23 Z. Zheng, H. Ji, Y. Zhang, J. Cai and C. Mo, *Solid State Ionics*, 2022, **377**, 115872.
24 H. Yao, P. Wang, M. Zhu and X. Shi, *Dalton Trans.*, 2024, DOI: **10.1039/D3DT03820C**.
25 Z. Peng, Q. Zhang, G. Qi, H. Zhang, Q. Liu, G. Hu, J. Luo and X. Liu, *Chin. J. Struct. Chem.*, 2024, **43**, 100191.
26 K. Zhang and R. Zou, *Small*, 2021, **17**, 2100129.
27 F. Zeng, C. Mebrahtu, L. Liao, A. K. Beine and R. Palkovits, *J. Energy Chem.*, 2022, **69**, 301–329.
28 Q. Zhang, K. Lian, Q. Liu, G. Qi, S. Zhang, J. Luo and X. Liu, *J. Colloid Interface Sci.*, 2023, **646**, 844–854.
29 M. Chen, N. Kitiphatpiboon, C. Feng, Q. Zhao, A. Abudula, Y. Ma, K. Yan and G. Guan, *Appl. Catal., B*, 2023, **330**, 122577.
30 M. V. Kante, M. L. Weber, S. Ni, I. C. van den Bosch, E. van der Minne, L. Heymann, L. J. Falling, N. Gauquelin, M. Tsvetanova and D. M. Cunha, *ACS Nano*, 2023, **17**, 5329–5339.
31 Z. Sun, Y. Zhao, C. Sun, Q. Ni, C. Wang and H. Jin, *Chem. Eng. J.*, 2022, **431**, 133448.
32 S. Khan, J. Arshad, I. Arshad, S. Aftab, S. S. Shah, S.-L. Lee, N. K. Janjua, K. Yusuf and H. Li, *Int. J. Hydrogen Energy*, 2024, DOI: **10.1016/j.ijhydene.2024.02.293**.
33 J. Arshad, N. K. Janjua and R. Raza, *J. Electrochem. Sci. Technol.*, 2021, **12**, 112–125.
34 H. He, P. Kou, Z. Zhang, D. Wang, R. Zheng, H. Sun, Y. Liu and Z. Wang, *J. Colloid Interface Sci.*, 2024, **653**, 179–188.
35 D. Wang, Z. Liu, S. Du, Y. Zhang, H. Li, Z. Xiao, W. Chen, R. Chen, Y. Wang and Y. Zou, *J. Mater. Chem. A*, 2019, **7**, 24211–24216.
36 F. Liu, M. Yu, X. Chen, J. Li, H. Liu and F. Cheng, *Chin. J. Catal.*, 2022, **43**, 122–129.
37 Y. Zhang, W. Dai, P. Zhang, T. Lu and Y. Pan, *J. Alloys Compd.*, 2021, **868**, 159064.
38 C. Duan, X. Li, D. Wang, Z. Wang, H. Sun, R. Zheng and Y. Liu, *Sustainable Energy Fuels*, 2022, **6**, 1479–1488.
39 Y. Lao, X. Huang, L. Liu, X. Mo, J. Huang, Y. Qin, Q. Mo, X. Hui, Z. Yang and W. Jiang, *Chem. Eng. J.*, 2024, **481**, 148428.
40 C. Feng, Y. Zhou, M. Chen, L. Zou, X. Li, X. An, Q. Zhao, P. Xiaokaiti, A. Abudula and K. Yan, *Appl. Catal., B*, 2024, **349**, 123875.
41 M. Han, C. Wang, J. Zhong, J. Han, N. Wang, A. Seifitokaldani, Y. Yu, Y. Liu, X. Sun and A. Vomiero, *Appl. Catal., B*, 2022, **301**, 120764.
42 S. Jiang, K. Tian, X. Li, C. Duan, D. Wang, Z. Wang, H. Sun, R. Zheng and Y. Liu, *J. Colloid Interface Sci.*, 2022, **606**, 635–644.
43 T. M. Butt, A. Ullah and N. K. J. Janjua, *J. Electroanal. Chem.*, 2022, **907**, 116053.
44 L. He, N. Wang, B. Sun, L. Zhong, M. Yao, W. Hu and S. Komarneni, *J. Cleaner Prod.*, 2022, **356**, 131680.
45 D. Berardan, A. Meena, S. Franger, C. Herrero and N. Dragoe, *J. Alloys Compd.*, 2017, **704**, 693–700.
46 W. Rong, Y. Chen, R. Dang, K. Huang, J. Xia, B. Zhang, J. Liu, H. Meng, Q. Cao and J. Wu, *J. Alloys Compd.*, 2024, **971**, 172786.
47 S. Kurumada, R. Yamanashi, K. Sugita, K. Kubota, H. Ito, S. Ikemoto, C. Chen, T. Moriyama, S. Muratsugu and M. Tada, *Chem. – Eur. J.*, 2024, e202303073.
48 K. Miao, W. Jiang, Z. Chen, Y. Luo, D. Xiang, C. Wang and X. Kang, *Adv. Mater.*, 2024, **36**, 2308490.
49 L. Yan, Y. Ren, X. Zhang, Y. Sun, J. Ning, Y. Zhong, B. Teng and Y. Hu, *Nanoscale*, 2019, **11**, 20797–20808.
50 D. Wang, C. Duan, Y. Yu, X. Li, Z. Wang, Y. Liu and C. Liu, *J. Alloys Compd.*, 2023, **967**, 171758.
51 W. Hooch Antink, S. Lee, H. S. Lee, H. Shin, T. Y. Yoo, W. Ko, J. Shim, G. Na, Y. E. Sung and T. Hyeon, *Adv. Funct. Mater.*, 2024, **34**, 2309438.
52 J. Li, D. Chu, H. Dong, D. R. Baker and R. Jiang, *J. Am. Chem. Soc.*, 2019, **142**, 50–54.
53 X. Bo, R. K. Hocking, S. Zhou, Y. Li, X. Chen, J. Zhuang, Y. Du and C. Zhao, *Energy Environ. Sci.*, 2020, **13**, 4225–4237.
54 S. Jain, J. Shah, N. S. Negi, C. Sharma and R. K. Kotnala, *Int. J. Energy Res.*, 2019, **43**, 4743–4755.
55 M. Asim, A. Hussain, S. Khan, J. Arshad, T. M. Butt, A. Hana, M. Munawar, F. Saira, M. Rani and A. Mahmood, *Molecules*, 2022, **27**, 5951.
56 T. M. Butt, N. K. Janjua, A. Mujtaba, S. A. Zaman, R. Ansir, A. Rafique, P. Sumreen, M. Mukhtar, M. Pervaiz and A. Yaqub, *J. Electrochem. Soc.*, 2020, **167**, 026503.
57 M. Asim, A. Hussain, M. Samancı, N. K. Janjua and A. Bayrakçeken, *Carbon Lett.*, 2024, 1–23.
58 C. Liu and L. Feng, *Chin. J. Struct. Chem.*, 2023, 100136.
59 C. Triolo, S. Schweidler, L. Lin, G. Pagot, V. Di Noto, B. Breitung and S. Santangelo, *Energy Adv.*, 2023, **2**, 667–678.
60 J. Wang, J. Zhang, L. Zhang, L. Chen, G. He and H. Jiang, *Appl. Catal., B*, 2024, **342**, 123382.
61 F. Liu, J. Dang, C. Zhao, B. Yuan, H. Qiu, Q. Wang, C. Zhang, L. Xiao, H. Miao and J. Yuan, *J. Alloys Compd.*, 2024, 173745.

62 A. Farooq, S. Khalil, B. Basha, A. Habib, M. Al-Buriahi, M. F. Warsi, S. Yousaf and M. Shahid, *Int. J. Hydrogen Energy*, 2024, **51**, 1318–1332.
63 S. Khan, A. Ahmad, R. R. Karri, M. Ouladsmane, N. K. Janjua and H. Li, *Int. J. Hydrogen Energy*, 2024, **52**, 1206–1216.
64 A. V. Saghir, S. M. Beidokhti and J. V. Khaki, *Ceram. Int.*, 2024, DOI: **10.1016/j.ceramint.2024.04.139**.
65 K. S. Sairam, S. T. Aziz, I. Karajagi, A. Saini, M. Pal, P. C. Ghosh and A. Dutta, *Int. J. Hydrogen Energy*, 2023, **48**, 10521–10531.
66 P. Amarnath, R. Madhu, K. Praveen, S. Govindarajan, S. Kundu and Y. Subramaniam, *ACS Appl. Energy Mater.*, 2023, **6**, 5899–5911.
67 P. Yang, Y. An, C. Feng, Y. Liu, S. Liu, L. Gao, Y. Zhou, X. Li, P. Li and F. Zeng, *Int. J. Hydrogen Energy*, 2024, **51**, 1218–1228.